CrystEngComm

ROYAL SOCIETY OF CHEMISTRY

HIGHLIGHT

View Article Online
View Journal | View Issue

Cite this: *CrystEngComm*, 2025, **27**, 5389

Crystal engineering of rare earth heteroleptic complexes: phosphine oxide ligand control, POM-directed assembly, and performance metrics

Jian-Jie Xu,†[a] Lin-Lin Wang,†[ab] Ying-Long Wang,†[a] Gui-Xiong Guo,†[a] Jian-Ming Liu,[c] Li-Xiong Dai, *[d] Min Liu[e] and Qiong-Hua Jin *[abf]

This study explores crystal engineering strategies for rare earth heteroleptic complexes, focusing on ligand design, supramolecular control, and functional performance. Phosphine oxide ligands (TPPO) synergize steric/electronic effects to stabilize coordination geometries, while mixed-ligand systems (*e.g.*, TPPO/phen) enhance Eu^{3+} luminescence (26.88% quantum yield). Polyoxometalates (POMs) template 3D architectures *via* hydrogen/charge interactions, enabling >95% photocatalytic dye degradation and >200 °C thermal stability. Rare earth-transition metal systems integrate 2D/3D topologies and multifunctionality (luminescence, gas adsorption) through electronic coupling. Additionally, carbon-based oxygen ligand systems (*e.g.*, β-diketonates) demonstrate the applicability of these core strategies—leveraging synergistic N-donor coordination and supramolecular interactions to achieve advanced functionalities like temperature-responsive luminescence. Future work will prioritize flexible ligand engineering and stimuli-responsive designs for applications in clean energy and quantum technologies, establishing a roadmap for advanced rare earth materials.

Received 30th April 2025,
Accepted 9th July 2025

DOI: 10.1039/d5ce00455a

rsc.li/crystengcomm

Introduction

The rare earth elements include the lanthanide series, scandium, and yttrium, totaling 17 elements.[1] The electronic configurations of these lanthanides are $[Xe]4f^n5d^16s^2$, where n ranges from 1 to 14 for cerium to lutetium. Scandium and yttrium, lacking 4f electrons, have outer electron configurations of $(n-1)dn^1s^2$, which are chemically similar to those of the lanthanide elements, thus they are also classified as rare earth elements.[2] Rare earth materials are extensively used in modern industry, earning them the name "industrial vitamins."[3,4] As a class of irreplaceable and critical materials, rare earths have infiltrated many high-tech sectors, driving technological advancements and industrial upgrades. Currently, the major focus areas in the rare earth industry include rare earth permanent magnets,[5,6] rare earth hydrogen storage materials,[7] rare earth laser materials,[8] and high-nuclearity lanthanide clusters.[9] These materials not only play a pivotal role in traditional sectors like electronics,[10] aerospace,[11] and energy,[12] but also show tremendous potential in emerging fields such as healthcare[13,14]and renewable energy.[15] For instance, rare earth permanent magnets are crucial for enhancing the efficiency and environmental performance of electric vehicles and medical equipment.[16,17] Rare earth materials exhibit unique advantages in efficient sensing applications. For instance, Eu^{3+}/Tb^{3+}-functionalized metal–organic frameworks (MOFs) demonstrate exceptional sensitivity for detecting phenylglycine and adrenaline in biofluids, with detection limits as low as 2.59–3.06 ng mL^{-1}.[18,19] Rare earth hydrogen storage materials are essential for the future hydrogen economy, facilitating safer and more efficient hydrogen storage and transportation, thus promoting the adoption of clean energy.[20,21]

As a fundamental discipline in rare earth applications, crystallographic engineering serves as the cornerstone for advancing these elements' functionalities.[22] This discipline not only provides a methodological framework for material optimization but also bridges molecular-level design with macroscopic functionalities, forming the technical foundation

[a] *Department of Chemistry, Capital Normal University, Beijing 100048, China. E-mail: jinqh@cnu.edu.cn, jinqh204@163.com*
[b] *College of Resource Environment and Tourism, Capital Normal University, Beijing 100048, China*
[c] *School of Mathematical Sciences, Peking University, Beijing 100871, China*
[d] *Wenzhou Institute, University of Chinese Academy of Sciences, Wenzhou, 325000, China*
[e] *Laboratory of Advanced Functional Materials, Ministry of Education, Faculty of Materials and Manufacturing, Beijing University of Technology, Beijing 100124, China*
[f] *State Key Laboratory of Rare Earth Resource Utilization, Changchun 130022, China*

† Jian-Jie Xu and Lin-Lin Wang are responsible for the content of the manuscript; Ying-Long Wang and Gui-Xiong Guo are mainly responsible for the drawing of pictures and the polishing of the content of the article. The four authors contributed equally in terms of workload.

for next-generation quantum devices, smart materials, and sustainable energy technologies. Guided by the hard and soft acid–base (HSAB) principle, rare earth ions exhibit preferential coordination with oxygen-donor ligands, though nitrogen-containing soft bases can participate in complex formation under specific conditions.[23] Crucially, the precise tuning of functional properties requires meticulous crystal engineering, where phosphorus-oxygen ligands have emerged as pivotal building blocks, leveraging their dual advantages of robust coordination strength and tunable steric/electronic configurations. Systematic modulation of ligand substituents enables precise control over coordination geometry and crystal field splitting through steric and electronic engineering. Recent breakthroughs employ nitrogen-containing co-ligands to establish P–O–N synergistic coordination systems, with this co-assembly strategy enhancing coordination saturation while optimizing energy transfer pathways, leading to remarkable improvements in both luminescent quantum yield and thermal stability. Moreover, hierarchical assembly control through supramolecular directing effects combined with polyoxometalate templates enables precise regulation of crystal packing modes, facilitating orderly organization across molecular to mesoscopic scales.[24,25] Looking forward, the engineering of rare earth-transition metal heteronuclear systems represents a promising frontier, where these hybrid architectures exploit intermetallic electronic coupling and spatial synergy to overcome single-component limitations, paving the way for multifunctional materials with tailored optoelectronic–magnetic properties.[26,27]As summarized in Table 1, our crystal engineering strategies overcome key limitations of current systems through synergistic ligand design, supramolecular templating, and heterometallic integration, achieving unprecedented precision in coordination control, stability under harsh conditions, and multifunctional performance.

Phosphine oxide ligands: steric and electronic effects

According to the soft and hard acid–base (SHAB) theory, the basicity of phosphine oxide compounds is governed by substituent type, which directly modulates their coordination capability. In protonic solvents, the basicity of R_3PO ligands is primarily dominated by solvent solvation effects, while inductive effects from phosphorus-bound substituents are negligible. For example, when MeR_2PO acts as a ligand, its basicity decreases in the order Me > Bu > ^{t}Bu. Conversely, in the gas phase, the inductive effects of R substituents dominate, leading to a reversed trend: $^i Pr_3PO > Et_3PO > Me_3PO$.[28] TPPO has found widespread application in the synthesis of high-performance materials.[29] In the case of the classical phosphorus-oxygen ligand TPPO, both spatial and electronic effects synergistically regulate the coordination geometry and topological structure of lanthanide complexes. The bulky triphenyl groups impose steric constraints, driving a systematic reduction in coordination numbers that correlates with lanthanide contraction. For early lanthanides (La^{3+}, Ce^{3+}; ionic radii ~1.1 Å), four TPPO ligands and three nitrates coordinate to form nine-coordinate complexes (*e.g.*, $[La(TPPO)_4(\eta^2\text{-}NO_3)_2(\eta^1\text{-}NO_3)]$) (Fig. 1).[30] The strong σ-donor ability of TPPO stabilizes metal–ligand bonds through P═O coordination, while the interplay between steric and electronic effects dictates the coexistence of bidentate and monodentate nitrates. For smaller lanthanides (Tb^{3+}–Lu^{3+}; radii <1.0 Å),[31] steric compression induced by TPPO reduces the coordination number to eight, retaining two bidentate nitrates and one unbound anion (*e.g.*, $[Lu(TPPO)_4(\eta^2\text{-}NO_3)_2]NO_3$). Concurrently, the contraction of P═O bond lengths (La–O: 2.545 Å → Lu–O: 2.200 Å) reflects enhanced electronic interactions. Crystallographic analysis reveals that the phenyl groups of TPPO drive layered stacking *via* π–π interactions ($d_{\pi-\pi} \approx$ 3.3–3.5 Å), while solvent-mediated hydrogen bonds stabilize the three-dimensional framework (Fig. 2).[32] This dual-control mechanism—steric dominance in dictating coordination numbers combined with electronic tuning of bond stability—provides a framework for designing lanthanide materials with tailored selectivity.

TPPO, a prototypical monodentate ligand, exhibits exceptional coordination versatility and luminescent tunability in lanthanide chemistry. However, the intrinsic coordination uniformity of monophosphine oxide ligands—restricted to monodentate or bridging modes—limits precise modulation of crystalline topology and functional properties in crystal engineering. Recent studies emphasize the unique advantages of diphosphine oxide ligands, which exhibit bimetallic coordination synergy. Their bis-phosphinate moieties enable versatile chelation or bridging modes, while

Table 1 Chapter-wise crystal engineering strategies and functional advances

Regulation strategy	Key methods	Advantageous outcomes
Steric–electronic synergy control	• TPPO substituent tuning (phenyl bulk) • Diphosphine oxide chain length modulation (C2–C6) • Anion-dependent coordination (NO_3^- *vs.* OTf^-)	• Precise coordination number control (8–10) • Ln^{3+} ionic radius-adaptive geometries • Layered stacking *via* π–π (d = 3.3–3.5 Å)
Hard–soft donor integration	• P═O/N-donor (phen) co-assembly • Solvent-driven coordination switching (MeCN *vs.* EtOH) • Rigid scaffold design (phen–phosphonates)	• Quantum yield boost (Eu^{3+}: Φ = 26.88%) • Over 99.5% Am(III) separation in 3–4 M HNO_3 • Thermal stability >250 °C
POM-templated hierarchical assembly	• H-bond/charge-directed 3D frameworks • Solvothermal synthesis ($MeCN/H_2O$ or $EtOH/H_2O$) • POM–Ln^{3+} charge-transfer engineering	• Over 95% photocatalytic dye degradation • Single-molecule magnets (U_{eff}/K_B = 386 K) • Thermal resilience >200 °C

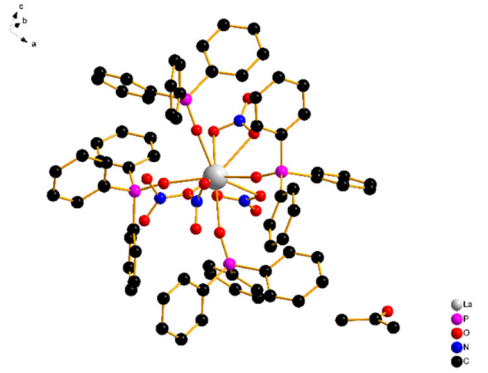

Fig. 1 $[La(TPPO)_4(\eta^2\text{-}NO_3)_2(\eta^1\text{-}NO_3)]$.

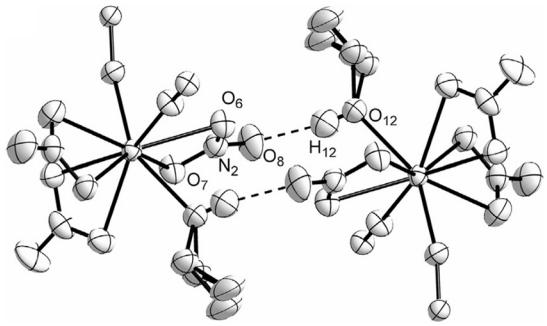

Fig. 2 Hydrogen bonding interactions in complex $[Tb(TPPO_3)_2(C_2H_5OH)(NO_3)_3]$. Hydrogen atoms and phenyl groups of TPPO are omitted for clarity.

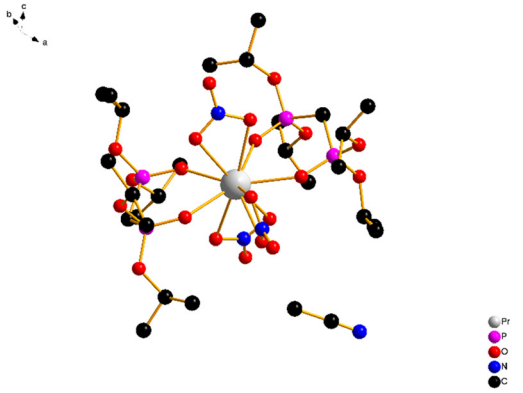

Fig. 3 $[Ln(NO_3)_3L_2]$.

spacers (alkyl/aryl groups) modulate ligand flexibility and steric bulk, thereby enabling multidimensional control over lanthanide coordination spheres, crystalline architectures, and optoelectronic properties. Although prior studies have identified isolated structural determinants (*e.g.*, ligand chain length), comprehensive structure–function correlations for diphosphine oxides remain underdeveloped. Key knowledge gaps include the mechanistic interplay between chain length/flexibility and coordination mode selection, geometric control *via* rigidity-flexibility balance, and cooperative effects of metal ionic radii and anion characteristics on topological differentiation. Through comparative analysis of lanthanide salt assemblies with diphosphine oxides spanning chain lengths (C2–C6) and rigidity motifs (*ortho*-phenylene *vs.* methylene), this study systematically deciphers structure-directing principles in crystal engineering. These findings establish a conceptual framework for the rational design of functional lanthanide supramolecular architectures. The structural features of tetraisopropoxymethylbis(phosphinate) (L = $(^iPrO)_2P(O)CH_2P(O)(O^iPr)_2$), a mid-length diphosphine oxide, exemplify ligand structure-coordination behavior correlations in lanthanide complexes. This ligand synergizes the potent electron-donating capacity of isopropoxy groups with the flexibility of a methylene bridge. The isopropoxy moieties enhance P═O coordination potency through inductive effects, while their steric bulk prevents packing defects caused by excessive chelation. Simultaneously, the methylene C–C σ-bond permits ~120° torsional flexibility, dynamically modulating the equilibrium between chelation and bridging modes. In nitrate systems ($Ln(NO_3)_3$), bidentate chelation yields ten-coordinate neutral complexes $[Ln(NO_3)_3L_2]$ (Ln = Ce, Pr, Nd) (Fig. 3). The high denticity of nitrate anions (bidentate) and ligand rigidity synergistically stabilize geometries best described as sphenocorona or bicapped square antiprisms.[33] When nitrate is replaced by weakly coordinating triflate (OTf^-), the rigid ligand L maintains bidentate chelation, while two OTf^- anions bind monodentately. This coordination mode, combined with two aqua ligands and two monodentate OTf^-, forms eight-coordinate ionic complexes $[Ln(OTf)_2L_2(H_2O)_2]^+OTf^-$ (Ln = La, Pr, Nd). At a 4 : 1 L : Ln ratio, four L ligands chelate the lanthanide center *via* their phosphinate oxygens, forming homoleptic $[LaL_4]^{3+}$ species with eight-coordinate square antiprismatic geometry.[34] These adopt an eight-coordinate square antiprismatic geometry solely through phosphinate oxygen coordination, demonstrating how ligand rigidity dictates coordination saturation. The lanthanide contraction effect significantly modulates coordination numbers: larger early lanthanides (La^{3+}, Ce^{3+}; ~1.1 Å) form nine-coordinate $[LnL_2(H_2O)_4Cl]Cl_2$, while smaller late lanthanides (Sm^{3+}, Eu^{3+}; ~0.96 Å) adopt eight-coordinate $[LnL_2(H_2O)_4]Cl_3$.[35] For intermediate Pr^{3+}, coexisting nine- and eight-coordinate isomers ($[PrL_2(OH)_2(H_2O)Cl][PrL_2(H_2O)_4Cl]Cl_2$) arise through hydroxo bridging, highlighting the dynamic interplay between ligand flexibility and metal ionic size in coordination mode selection. Collectively, these results demonstrate that precise control of diphosphine oxide electronic properties, bridge lengths, and flexibility parameters enables tailored engineering—from discrete complexes to extended frameworks—thereby establishing foundational principles for programmable lanthanide material design (Fig. 4).

Alternative diphosphine oxides exhibit multidimensional structure–function correlations in modulating lanthanide coordination spheres and designing crystalline topologies, governed by steric–electronic cooperativity. Ligand chain length

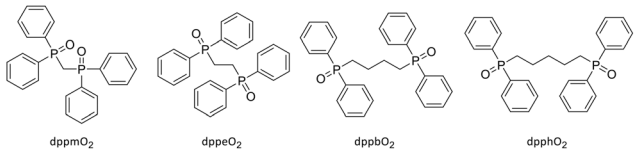

Fig. 4 $dppmO_2$ and $dppeO_2$.

and stiffness critically dictate coordination behavior. Compact rigid ligands such as $dppmO_2$ (bis(diphenylphosphine oxide) methane),[36] with limited bite angles (~70°), fail to bridge lanthanide centers, forming only chelated molecular species. In contrast, medium-length ligands like $dppeO_2$ (bis(diphenylphosphine oxide)ethane) enable dynamic bridging, constructing 2D lamellar polymers (*e.g.*, $[Pr(NO_3)_3(dppeO_2)_{1.5}]_n$).[37] However, extending the chain length to four carbons as in $dppbO_2$ (bis(diphenylphosphino)butane dioxide) reverses this trend: solvothermal reactions yield strictly binuclear complexes $[(dppbO_2)_2Ln(NO_3)_3(\mu\text{-}dppbO_2)Ln(NO_3)_3(dppbO_2)]$ (Ln = Pr, Nd, Sm, Dy), crystallizing in monoclinic $P2_1/n$ space groups.[38] The flexible $(CH_2)_4$ backbone of $dppbO_2$ promotes chelation over bridging, as evidenced by *syn*-conformation of P═O groups in chelate rings (O–P–C angles ~112.8°) *versus* *anti*-conformation in bridging modes. This contrasts sharply with $dppeO_2$'s polymeric architectures, where shorter ligand length enforces bridging coordination. The resulting topologies (grid, herringbone, or hexagonal) are further modulated by anion identity (NO_3^- *vs.* Cl^-) and synthetic methods. In nitrate complexes, larger early lanthanides (Pr^{3+}, Nd^{3+}; ~1.1 Å) form nine-coordinate T-junctions, yielding corrugated lamellae with d-spacing ~12.8 Å. In contrast, chloride analogues (*e.g.*, $[NdCl_3(dppeO_2)_{1.5}]_n$) assemble into orderly brick-like structures (*d*-spacing ~13.8 Å), attributed to Cl^-'s low denticity. Extended flexible ligands such as $dpphO_2$ (bis(diphenylphosphino)hexane dioxide) exemplify structural adaptability, achieving exceptional emission lifetimes (3.73 ms) in $[Eu(dpphO_2)_2Cl_2]^+Cl^-$ through hydrophobic shielding.[39] Collectively, diphosphine oxides provide atomically precise engineering paradigms for lanthanide complexes, enabling tailored architectures through synergistic control of chain dimensions, flexibility, and anion selection.

Mixed ligand strategies: synergistic coordination of phosphorus–oxygen and nitrogen donors

As prototypical rigid ligands, phenanthroline (phen) derivatives exhibit unique architectural control in lanthanide coordination chemistry, enabled by their planar conjugated structure and pre-organized N_2-donor system.[40] Their conformationally rigid framework stabilizes metal coordination geometries and directs supramolecular ordering through π–π interactions. However, traditional phen ligands face limitations in coordination strength and selectivity. The incorporation of phosphine oxide (P═O) moieties addresses these challenges, opening new

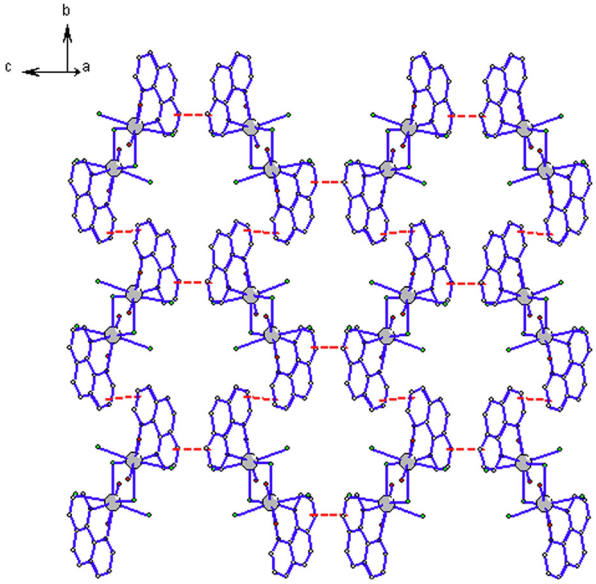

Fig. 5 Schematic representation of the two-dimensional mesh 6^3 topology formed by π–π interactions.

avenues for molecular engineering. Phosphine oxide functionalities synergize strong coordination capability with electronic tunability. Their lone pairs effectively satisfy the high coordination demands of lanthanides, while substituent steric effects enable Ångstrom-scale spatial precision.

For example, in the Ce(III)-based dinuclear complex $[(CeCl_2L(phen))_2(\mu\text{-}Cl)_2]\cdot CH_3CN$,[41] the Ce^{3+} center adopts an eight-coordinate geometry coordinated by two P═O oxygens (from ligand L), two phen nitrogens, and bridging chloride ions. This assembly forms a 2D 6^3 topological framework stabilized by π–π stacking interactions between adjacent phen ligands (Fig. 5).

In contrast, mononuclear complexes $[LnCl(H_2O)_3L(phen)]\cdot nCH_3CN$ (Ln = Dy–Lu)[41] form 2D 4.8^2 hydrogen-bonded networks *via* C–H···Cl and O–H···Cl interactions. This structural divergence underscores the dual influence of solvent effects and lanthanide contraction on coordination numbers (8–9) and framework dimensionality. Similarly, TPPO–phen hybrid systems exhibit solvent-dependent coordination patterns. In acetonitrile, ten-coordinate complexes $[Ln(TPPO)_2(phen)(NO_3)_3]$ (Ln = Ce, Gd, Tb, Ho, Eu)[32] form, stabilized by dual π–π interactions (phen–phen and TPPO–phenyl). In ethanol, nine-coordinate species $[Ln(TPPO)_2(C_2H_5OH)(NO_3)_3]$ (Ln = Tb–Tm)[32] dominate, with $R_2^2(12)$ hydrogen bonds enhancing stability (Fig. 6). Notably, phen's steric rigidity enhances luminescence efficiency in Tb^{3+} and Eu^{3+} complexes (quantum yields: 11.36–26.88%; lifetimes: 1.10–1.14 ms) by suppressing non-radiative quenching. In contrast, ethanol-coordinated analogs show reduced performance due to O–H vibrational deactivation. These studies highlight the critical interplay between ligand architecture, supramolecular interactions (hydrogen bonding, π-stacking), and lanthanide ionic radii, which collectively govern structural diversity, thermal stability, and photophysical properties. This synergy provides a blueprint for the rational design of multifunctional lanthanide materials.

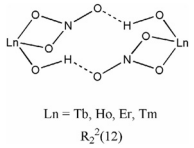

Fig. 6 $R_2^2(12)$ hydrogen bonds in complexes $[Ln(TPPO)_2(C_2H_5OH)(NO_3)_3]$ (Ln = Tb–Tm).

The integration of phen frameworks with phosphine oxides creates a "hard–soft" coordination microenvironment, where phen's pre-organized N-donors minimize entropic penalties, and the flexible P═O groups adapt to lanthanide ionic radii and electronic configurations. This mixed-ligand strategy expands structural diversity (*e.g.*, anion-regulated 1 : 1 ↔ 1 : 2 stoichiometry) and enables precise microenvironment engineering through electronic-spatial synergy, advancing the design of lanthanide systems with tailored functionalities. For example, in $[Eu(TPPO)_2(phen)(NO_3)_3]$, phen's rigid chelation suppresses nonradiative decay, achieving a quantum yield of 26.88% and a $^3D_0$ lifetime of 1.14 ms. Contrastingly, ethanol-coordinated $[Tb(TPPO)_2(C_2H_5OH)(NO_3)_3]$ shows reduced performance (Φ = 2.16%), underscoring phen's photophysical superiority. Structural studies reveal P═O→Ln^{3+} bonding (*e.g.*, Ce–O = 2.622 Å in $[Ce(TPPO)_2(phen)(NO_3)_3]$) and topology-defining interactions (π–π stacking: 3.29–3.47 Å; H-bonding), which confer thermal stability (>250 °C). Solvent-controlled assembly (acetonitrile *vs.* ethanol) further modulates coordination modes (Fig. 7).

Advanced ligands merging phen's N-donors with phosphonate O-donors enhance Am(III)/Eu(III) selectivity *via* hybrid covalent-ionic bonding. Branched phen–phosphonates (*e.g.*, C2–POPhen)[42] exhibit improved Am(III) separation (SF = 14 *vs.* 7 for linear analogues), supported by shorter Am–N bonds (2.607–2.639 Å *vs.* Eu–N: 2.650–2.698 Å) and higher Mayer bond orders (Am–N: 0.247–0.250). Phosphonate P═O groups stabilize Eu complexes electrostatically (Eu–O = 2.374–2.378 Å), demonstrating a dual bonding strategy for nuclear waste applications. These insights establish a roadmap for designing multifunctional lanthanide materials with programmable photophysical, catalytic, and separative properties. The Ph_2-BPPhen[43] ligand validates the broad applicability of this strategy, where structural characterizations reveal that the N_2O_2 tetradentate coordination mode of phen enforces deep metal encapsulation, while the phosphonate group contributes strong binding affinity ($\log\beta$ = 7.26) to ensure complex stability. In nitric acid media, the system achieves >99.5% Am(III) recovery

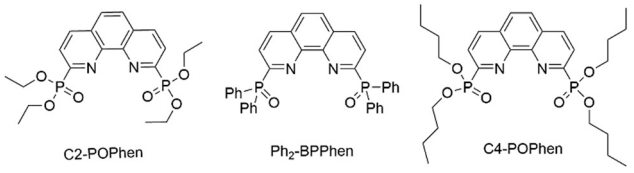

Fig. 7 *ortho*-Phenylphenol derivatives.

efficiency, with favorable kinetic parameters (activation energy E^a = 0.3 eV, equilibrium time t^{eq} < 2 min) highlighting the advantage of the rigid scaffold in enabling rapid complexation. Subsequent work by Yang[44] elucidated anion-regulated speciation: ClO_4^- anions facilitate 1 : 2 C4–POPhen complex formation, whereas competitive NO_3^- binding restricts stoichiometry to 1 : 1 through anion exchange processes, consistent with Matveev's observations of 2 : 1 complex dominance at high concentrations (>10^{-3} M). Quantum chemical calculations reveal significant 5f-N π* covalent interactions in americium complexes (WBI = 0.351), contrasting with the localized 4f orbitals and predominantly ionic oxygen bonding in europium analogues (WBI = 0.312), establishing the quantum mechanical basis for selectivity. This molecular engineering approach demonstrates remarkable efficacy under simulated high-level liquid waste (HLLW) conditions (3–4 M HNO_3), where sterically optimized phen–phosphonates exhibit 5-fold higher Am(III) separation factors than conventional HDEHP extractants, propelling actinide/lanthanide separation into an era of sustainable precision chemistry.

Supramolecular control in crystal packing

Supramolecular paradigms enable dynamically switchable assembly in crystalline architectures through non-covalent interactions (*e.g.*, hydrogen bonding, π-stacking, van der Waals forces, and ionic interactions), establishing a foundation for atomic-level lattice engineering.[45] These approaches allow dual stabilization of metal–ligand frameworks and precise control over structural parameters (*e.g.*, pore geometry, dimensionality, and symmetry), thereby optimizing functionalities in catalysis,[46] adsorption,[47] and photoresponsive systems.[48] In contrast, traditional coordination architectures, limited by rigid ligands or uniform interaction modes, often fail to attain metastable equilibria within complex supramolecular matrices. To address these challenges, POMs[49]—nanoscale clusters of transition metal ions and oxygen atoms—have emerged as supramolecular directors.[50] Their structural uniqueness, exemplified by Keggin-type clusters (*e.g.*, α-$[PMo_{12}O_{40}]^{3-}$), leverages surface oxo groups as hydrogen-bond acceptors to construct 3D networks with phosphine oxides or solvents, enabling Ångström-level precision in lanthanide coordination. Concurrently, the high anionic charge density and dimensional adaptability of POMs facilitate charge-guided assembly, templating stable open-framework or lamellar architectures through Coulombic interactions. Recent advances in POM–Ln^{3+} hybrid systems demonstrate synergistic charge-transfer cooperativity, tailoring bandgap engineering (E_g ≈ 2.5–3.0 eV) to suppress exciton recombination and achieve exceptional photocatalytic performance (>95% dye degradation efficiency). This hierarchical integration—spanning coordination chemistry, supramolecular assembly, and electronic structure modulation—overcomes classical crystallization limitations, paving the way for molecular-to-bulk functional convergence in lanthanide-based materials.

Crystalline engineering in Ln^{3+}/phosphine oxide/POM ternary systems demonstrates multifaceted assembly strategies. Lanthanide centers (La–Er series) coordinated by TPPO or bisphosphonate ligands (L) and templated by Keggin-type POMs ($[XM_{12}O_{40}]^{n-}$) achieve structural diversity through supramolecular modulation. Solvothermal synthesis in MeCN/H_2O or EtOH/H_2O yields two distinct architectures: (i) TPPO-based complexes ($[Ln(TPPO)_4(H_2O)_3][POM]\cdot n$solvent)[51] adopt seven-coordinate distorted pentagonal bipyramidal geometries, where P═O chelation stabilizes Ln^{3+}, while POMs template 3D hydrogen-bonding/π-stacking networks (orthogonal or monoclinic porous frameworks) *via* O···π(arene) and solvent interactions; (ii) bisphosphonate derivatives ($[LnL_3(H_2O)][POM]\cdot$solvent)[52] exhibit eight-coordinate geometries, utilizing flexible phosphonate bite angles (105–120°) to accommodate structural demands, while POMs direct lamellar or chain-like architectures ($P2_1/c$ or $P\bar{1}$ space groups) *via* O–H···O (alkyl) hydrogen bonding. In both systems, POMs act as supramolecular templates: the aromatic bulk of TPPO promotes dense 3D hydrogen-bond networks (9H-bonds per unit cell in Fig. 8),[53] whereas the conformational flexibility of L enables open-channel architectures (C–H···O interlamellar linkages in Fig. 9), modulating crystallographic packing coefficients (0.65–0.78). Solvent engineering (MeCN *vs.* EtOH) and POM composition (Mo–O 1.71 Å *vs.* W–O 1.79 Å) precisely tune interactions, evidenced by THz spectral shifts (POM peaks 0.23–0.32 THz redshift with H-bond strength; TPPO@1.20 THz *vs.* L@1.05 THz rigidity correlation). These architectures exhibit exceptional photocatalytic efficiency (>95% dye degradation under visible light), where POM–Ln^{3+} charge-transfer cooperativity tailors bandgaps (2.49–3.05 eV by UV-vis). PVDF immobilization resolves recyclability issues (5 cycles with <5% efficiency loss), while thermal resilience (>200 °C by TGA) enables high-temperature catalytic applications, establishing a robust platform for functional lanthanide material design.

Supramolecular assembly of Dy^{3+}/TPPO/POM systems generates two single-molecule magnet (SMM) prototypes: co-crystalline 1Dy and POM-coordinated 2Dy, illustrating how the interplay between coordination chemistry and supramolecular

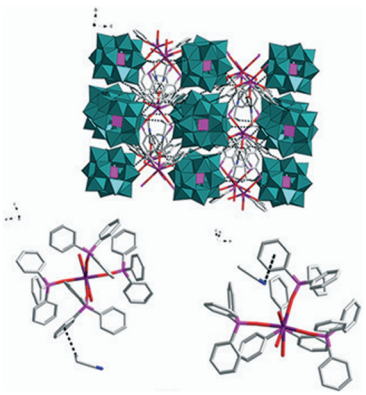

Fig. 8 The crystal stacking of complex $[Nd(TPPO)_4(H_2O)_3](PMo_{12}O_{40})\cdot 4CH_3CN$.

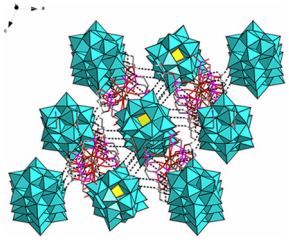

Fig. 9 The crystal stacking of complex $[DyL_3(H_2O)]PW_{12}O_{40}\cdot CH_3CN$.

engineering diversifies magnetic architectures. In 1Dy, Dy^{3+} adopts a pseudo-pentagonal bipyramidal (PBP) geometry (CShM = 0.976), with axial TPPO ligands (Dy–O = 2.249 Å) and equatorial H_2O/TPPO coordination. The orthorhombic lattice (Pbcn) is constructed through H_2O→POM hydrogen bonds (O···O = 2.846 Å) and arene π-stacking (interplanar distance 3.753 Å), enforcing Dy···Dy separations of 13.87 Å to suppress intermagnetic coupling. In contrast, hydrothermal synthesis of 2Dy yields POM-coordinated Dy^{3+} in a near-ideal PBP geometry (CShM = 0.221), with contracted axial Dy–O bonds (2.201 Å) enhancing magnetic anisotropy. Its monoclinic lattice ($P2_1/n$) features seven-membered H-bonded POM–Dy rings (O···O = 2.68–2.91 Å) propagating as 1D chains along the *a*-axis. These structural divergences dictate magnetic behavior: 1Dy exhibits Raman/direct relaxation (U_{eff}/K_B = 91 K at 2 kOe) due to equatorial TPPO steric effects, while 2Dy achieves zero-field U_{eff}/K_B = 310 K (enhanced to 386 K under 800 Oe) *via* Orbach relaxation, with POM-enhanced symmetry suppressing quantum tunneling of magnetization (QTM)—a record for POM-based SMMs. Luminescent properties further reflect supramolecular engineering: 1Dy shows dominant cryogenic π–π* (TPPO) emission, whereas 2Dy preserves Dy^{3+}-centered transitions (574 nm) through POM-mediated ligand-to-metal charge transfer (LMCT) sensitization, demonstrating photonic regulation *via* coordination microenvironments. Collectively, phosphine oxide ligand design, POM-directed non-covalent assembly, and solvation-controlled hierarchy enable atomically precise integration of magnetic and optical functionalities in supramolecular crystalline materials.

Extension to carbon-based oxygen ligand systems

Carbon-based oxygen ligands—encompassing carboxylates, β-diketonates, and phenolic derivatives—constitute a cornerstone of lanthanide coordination chemistry by providing robust, geometrically versatile scaffolds through their O-donor motifs. While their strong binding affinity ensures thermodynamic stability, the inherent limitations of homoleptic assemblies in structural diversification necessitate advanced engineering approaches. Therefore, there are also many synthetic ideas of carbon–oxygen complexes that meet the strategy of this paper, and have certain excellent properties.

From a crystal engineering perspective, the mixed coordination of β-diketonates with N-donor ligands significantly enhances functional properties of lanthanide complexes through precise control of coordination geometry and supramolecular assembly. In the work by Kitos *et al.*, 2-amidinopyridine (PyAm) as a rigid bidentate N-donor synergizes with acetylacetone (acac) to construct mononuclear [Ln(acac)$_3$(PyAm)] complexes (space group $P2_1/*n*$).[54] Critically, the amidinium group (–C(NH)NH$_2$) of PyAm drives 2D hydrogen-bonded networks *via* dual N–H···O=C(acac) interactions ($d \approx 2.8$ Å), which not only stabilizes the triangular dodecahedral coordination geometry but also enables temperature-responsive Stark sublevel splitting (S_r = 2.03% K^{-1} for Dy^{3+}), realizing molecular-level optical thermometry. Complementary work by Dar *et al.* demonstrates that pyrazine (pyz), acting as a monodentate ligand, replaces aqua ligands in [Ln(acac)$_3$] to form square-antiprismatic [Ln(acac)$_3$(pyz)$_2$] (Sparkle/PM3-optimized).[55] Crystal packing reveals enhanced intermolecular electronic coupling through C–H···π contacts ($d \approx 3.5$ Å) involving pyz's delocalized π-system, boosting the Eu^{3+} quantum yield by 20-fold (φ_{CHCl_3} = 1.17% *vs.* hydrated precursor) and enabling phase-dependent luminescence color tuning for Sm^{3+}/Eu^{3+} systems (CIE coordinate shift $\Delta*x*$ = 0.44). Collectively, these studies prove that the geometric constraints and supramolecular directing capabilities of N-donor ligands effectively compensate for the conformational flexibility of β-diketonates, establishing a new paradigm for designing highly stable and functional lanthanide crystalline materials. Polyoxometalate (POM)-based supramolecular templates offer a powerful strategy for directing the assembly of rare-earth heteroleptic complexes with carbon-based oxygen ligands. As demonstrated in luminescent dimeric oxalate-bridged Eu^{3+}/Tb^{3+} implanted arsenotungstates (*e.g.*, $K_{17}Na_2H_5[\{(As_2W_{19}O_{67}(H_2O))Ln(H_2O)_2\}_2(C_2O_4)]\cdot 87H_2O$ (Ln = Eu, Tb) (Fig. 10),[56] the rigid lacunary [As$_2$W$_{19}$O$_{67}$]$^{14-}$ polyanion acts as an inorganic scaffold that precisely positions lanthanide ions within its vacancy sites. The oxalate ligand ($C_2O_4^{2-}$), serving as an organic linker, bridges adjacent Ln^{3+} centers (Eu–Eu distance: 6.35 Å) to form a symmetric dimeric architecture with C_{2v} symmetry as Fig. 10. This supramolecular control not only stabilizes the coordination geometry (biaugmented trigonal prism) of Ln^{3+} ions but also facilitates efficient energy transfer between Tb^{3+} and Eu^{3+} centers, enabling tunable emission from green to red *via* codoping. Moreover, the synergistic integration of POM templates with oxalate ligands enhances photostability in aqueous media and creates oxygen-rich binding sites for selective Ba^{2+} sensing, underscoring the role of POM-directed supramolecular engineering in optimizing functional performance for sensing applications.

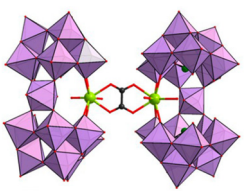

Fig. 10 Polyhedral/ball-and-stick representation of $K_{17}Na_2H_5[\{(As_2W_{19}O_{67}(H_2O))Ln(H_2O)_2\}_2(C_2O_4)]\cdot 87H_2O$.

Future directions: heterometallic coordination and advanced material design

In recent years, single metal-based MOFs (such as Zn, Ni)[57,58] have become a research hotspot in the field of porous materials due to their unique structural tunability and functional diversity. Due to the mixed regulation structure of metals and organic ligands, MOFs have unique properties in catalysis, sensing and other fields. However, there are still limitations in the functional integration and performance optimization of single-metal MOF materials. The mixed regulation of rare earth and transition metal crystal structure provides a new idea to break through these bottlenecks. Heterometallic frameworks achieve structural-functional dual-dimensional regulation through the synergistic coordination of rare earth and transition metals (such as Cu, Ag). At the structural level, rare earth ions often face the challenge of unsaturated coordination sites due to high coordination number requirements, while the low coordination number tendency (4–6) of d-zone transition metals can just fill this gap. Based on the HSAB, rare earth ions as hard acids preferentially bind to oxygen-containing hard base ligands (such as carboxylic acids, phosphine–oxygen groups), while transition metals tend to coordinate with sulfur/nitrogen-containing soft base ligands (such as thiols, pyridines). This principle is exemplified in the reactivity of rare-earth phosphinidene complexes (*e.g.*, [$L_3Ln_3(\mu_3$-$PC_6H_4)$]), where the soft P^{2-} ligand enables unique desulfurization and cyclization pathways with CS_2 through electronic coupling between Ln^{3+} and P centers.[59] By designing bifunctional ligands (such as organic molecules containing both carboxylic acid and thioether groups), heteronuclear coordination nodes can be accurately constructed.

The past decade has seen revolutionary breakthroughs in heterometallic framework design through crystal engineering paradigms. Strategic integration of 4f-lanthanide and 3d/4d-transition metal coordination chemistries with multidentate oxo-ligands (*e.g.*, DSPT, Hpdc, IN/Ox) has enabled precise construction of heterometallic architectures combining intricate topologies with programmable properties. Architectural diversity is achieved through molecular building block (MBB) engineering: bottom-up assembly creates 2D lamellar networks ($Ag_2(DSPT)_2$–$Ln_2(COO)_2$ (ref. 60) *via* 3.40 Å Ag···π contacts) to 3D open frameworks (Cu_4I_4–$Ln_2(COO)_4$ (ref. 61) cage topologies), demonstrating dimensional precision. Emergent topologies ((3,4,5)-connected networks, sqc-21/495 classifications) redefine dimensional constraints inherent to single-metal frameworks. Multifunctional integration is achieved through: (i) narrow-band lanthanide luminescence (Tb^{3+}: 545 nm $^5D_4 \rightarrow {}^7F_1$; Eu^{3+}:

614 nm $^5D_4 \rightarrow {}^7F_2$) coupled with d-metal charge transfer (Cu^+ MLCT);[62] (ii) micro/mesopore-engineered gas storage (1-Tb: 524 $m^2\ g^{-1}$ BET, CO_2 61.6 $cm^3\ g^{-1}$@273 K, H_2 110 $cm^3\ g^{-1}$@77 K); (iii) dynamic ion-exchange capabilities (96.5% $Cr_2O_7^{2-}$ capture efficiency). The interplay of weak forces (Ag–Ag 3.16 Å, Ag$\cdots\pi$ 3.40 Å) and ligand compliance (DSPT torsional angles = 50–66°) establishes innovative pathways for designing stimuli-adaptive frameworks. Next-generation frameworks will emerge from hierarchical control strategies: (i) electronic cooperativity in polynuclear clusters (Cu^+–Ln^{3+} CT pathways); (ii) ligand compliance engineering (photo-switchable $OPPh_2$–R); (iii) multicomponent co-assembly (ternary metal-cluster junctions). Such systems will unify thermal resilience (>300 °C decomposition), multistimuli responsiveness (photonic–electronic–magnetic coupling), and functional hybridization (catalytic-sensing-energetic unity), pioneering applications in sustainable energy technologies, environmental detoxification, and quantum information science.

Conclusions

The article systematically explores crystal engineering strategies for rare earth heteroleptic complexes, focusing on ligand design, supramolecular control, and functional applications. The study highlights that crystal engineering, through precise molecular-level design, regulates the coordination geometry, crystal topology, and macroscopic properties of rare earth complexes, thereby establishing a foundation for developing multifunctional materials. In ligand design, phosphorus–oxygen ligands such as TPPO significantly influence the coordination number and bonding stability of rare earth ions *via* steric hindrance and electronic modulation. For instance, the phenyl groups of TPPO facilitate layered stacking through π–π interactions, while its strong σ-donor capability enhances metal–ligand bond stability. Mixed-ligand strategies, such as integrating phosphorus–oxygen ligands with nitrogen-donor ligands (*e.g.*, phen, further optimize the luminescent performance of rare earth complexes. The rigid structure of phen suppresses non-radiative transitions, thereby elevating the quantum yield of europium (Eu^{3+}) complexes to 26.88%. Furthermore, the extension to carbon-based oxygen ligand systems (*e.g.*, carboxylates, β-diketonates) validates the universality of these engineering principles. Their synergistic combination with N-donor ligands enables precise control over coordination geometry and drives the formation of supramolecular networks (*e.g.*, 2D hydrogen-bonded frameworks *via* N-H$\cdots$O=C interactions), achieving functionalities such as molecular-level optical thermometry and significantly enhanced luminescence quantum yields. In supramolecular engineering, polyoxometalates (POMs) serve as structural templates, directing the assembly of three-dimensional porous or lamellar architectures *via* hydrogen bonding and charge-guided interactions. This approach significantly improves photocatalytic efficiency (>95% dye degradation) and thermal stability (>200 °C). Furthermore, rare earth-transition metal heteronuclear systems leverage soft–hard ligand synergy and electronic coupling to achieve multidimensional topologies (*e.g.*, 2D lamellar, 3D cage-like frameworks) and multifunctional integration, including luminescence, gas adsorption, and ion exchange. Future research should prioritize ligand flexibility modulation, intermetallic electronic cooperativity, and stimuli-responsive material design to advance applications in clean energy, environmental remediation, and quantum information technologies. This work provides a systematic theoretical framework and technical pathway for the rational design of rare earth functional materials.

Data availability

No primary research results, software or code have been included and no new data were generated or analysed as part of this review.

Conflicts of interest

There are no conflicts to declare.

Acknowledgements

This work has been supported by the National Natural Science Foundation of China (Grant No. 21171119), the Beijing Natural Science Foundation (Grant No. 2172017), the Key Project of Science and Technology Plan of Beijing Education Commission (No. KZ20231002808), the Key Laboratory of Functional Inorganic Material Chemistry (Heilongjiang University), Ministry of Education, and the Open Funds of the State Key Laboratory of Rare Earth Resource Utilization (RERU2023001).

Notes and references

1 V. Balaram, *Geosci. Front.*, 2019, **10**, 1285–1303.
2 N. Dushyantha, N. Batapola, I. M. S. K. Ilankoon, S. Rohitha, R. Premasiri, B. Abeysinghe, N. Ratnayake and K. Dissanayake, *Ore Geol. Rev.*, 2020, **122**, 103521.
3 H. Q. Wang, M. Batentschuk, A. Osvet, L. Pinna and C. J. Brabec, *Adv. Mater.*, 2011, **23**, 2675–2680.
4 L. Depraiter and S. Goutte, *Resour. Policy*, 2023, **86**, 104137.
5 S. Sugimoto, *J. Phys. D: Appl. Phys.*, 2011, **44**, 064001.
6 J. W. Zhang, X. M. Kan, B. Q. Liu, G. C. Liu, A. X. Tian and X. L. Wang, *Chem. – Eur. J.*, 2015, **21**, 16219–16228.
7 H. Zhang, X. Zheng, X. Tian, Y. Liu and X. Li, *Prog. Nat. Sci.: Mater. Int.*, 2017, **27**, 50–57.
8 A. Jha, B. Richards, G. Jose, T. Teddy-Fernandez, P. Joshi, X. Jiang and J. Lousteau, *Prog. Mater. Sci.*, 2012, **57**, 1426–1491.
9 X.-Y. Zheng, J. Xie, X.-J. Kong, L.-S. Long and L.-S. Zheng, *Coord. Chem. Rev.*, 2019, **378**, 222–236.
10 A. J. Steckl, J. C. Heikenfeld, L. Dong-Seon, M. J. Garter, C. C. Baker, W. Yongqiang and R. Jones, *IEEE J. Sel. Top. Quantum Electron.*, 2002, **8**, 749–766.
11 V. K. Sharma, V. Kumar and R. S. Joshi, *J. Mater. Res. Technol.*, 2019, **8**, 3504–3516.

12 L. Talens Peiró and G. Villalba Méndez, *JOM*, 2013, **65**, 1327–1340.
13 G. Bao, *J. Lumin.*, 2020, **228**, 117622.
14 S. Wu, Y. Lin, J. Liu, W. Shi, G. Yang and P. Cheng, *Adv. Funct. Mater.*, 2018, **28**, 1707169.
15 R. M. Almeida, N. Sousa, R. E. Rojas-Hernandez and L. F. Santos, *J. Sol-Gel Sci. Technol.*, 2020, **95**, 520–529.
16 A. Trench and J. P. Sykes, *Engineering*, 2020, **6**, 115–118.
17 J. M. D. Coey, *Engineering*, 2020, **6**, 119–131.
18 X. Liu, X. Li, W. Li, L. Liu, H. Ren, H. Jing, L. Zhang, J. Yin and L. Fan, *Microchem. J.*, 2024, **207**, 112127.
19 D. Zhao, W. Li, R. Wen, W. Li, X. Liu, X. Zhang and L. Fan, *J. Rare Earths*, 2024, **42**, 987–994.
20 C. Frommen, M. H. Sørby, M. Heere, T. D. Humphries, J. E. Olsen and B. C. Hauback, *Energies*, 2017, **10**(12), 2115.
21 F. Liang, J. Lin, Y. Cheng, D. Yin, Y. Wu and L. Wang, *Sci. China: Technol. Sci.*, 2018, **61**, 1309–1318.
22 G. R. Desiraju, *J. Am. Chem. Soc.*, 2013, **135**, 9952–9967.
23 J. Brugger, W. Liu, B. Etschmann, Y. Mei, D. M. Sherman and D. Testemale, *Chem. Geol.*, 2016, **447**, 219–253.
24 P. D. Beer and P. A. Gale, *Angew. Chem., Int. Ed.*, 2001, **40**, 486–516.
25 J. M. Lehn, *Angew. Chem., Int. Ed.*, 2003, **29**, 1304–1319.
26 E.-L. Zhou, C. Qin, D. Tian, X.-L. Wang, B.-X. Yang, L. Huang, K.-Z. Shao and Z.-M. Su, *J. Mater. Chem. C*, 2018, **6**, 7874–7879.
27 T. I. Masatomi Sakamotoa, M. Sato, S. Matsushima, M. Miwa, H. Aono and Y. Sadaoka, *J. Alloys Compd.*, 1997, **260**, 59–63.
28 A. W. G. Platt, *Coord. Chem. Rev.*, 2017, **340**, 62–78.
29 S. Stewart, R. Maloney and Y. Sun, *Chem. Commun.*, 2023, **59**, 3546–3549.
30 W. Levason, E. H. Newman and M. Webster, *Polyhedron*, 2000, **19**, 2697–2705.
31 Y. Ma, S. Xu, X. Wang, M. Liu, Y. X. Li, X. L. Xin and Q. H. Jin, *Z. Anorg. Allg. Chem.*, 2017, **643**, 780–788.
32 S. Xu, M. Liu, H.-L. Han, Z.-F. Li, Q.-H. Jin, J. Hou, W. Su, Y.-Y. Chen and J.-Y. Yao, *Polyhedron*, 2015, **85**, 69–75.
33 Q. Jin, L. Ricard and F. Nief, *Polyhedron*, 2005, **24**, 549–555.
34 S. Xu, M. Liu, Y.-P. Yang, Y.-H. Jiang, Z.-F. Li, Q.-H. Jin, X. Wang and X.-N. Xue, *Polyhedron*, 2015, **87**, 293–301.
35 Y. Ma, Y.-S. Yang, Y.-H. Jiang, Y.-X. Li, M. Liu, Z.-F. Li, H.-L. Han, Y.-P. Yang, X.-L. Xin and Q.-H. Jin, *RSC Adv.*, 2017, **7**, 41651–41666.
36 A. M. J. Lees and A. W. G. Platt, *Inorg. Chem.*, 2003, **42**, 4673–4679.
37 Z. Spichal, M. Necas and J. Pinkas, *Inorg. Chem.*, 2005, **44**, 2074–2080.
38 Z. Spichal, M. Necas, J. Pinkas and Z. Zdrahal, *Polyhedron*, 2006, **25**, 809–814.
39 Z. Spichal, V. Petricek, J. Pinkas and M. Necas, *Polyhedron*, 2008, **27**, 283–288.
40 S. A. Cotton, J. M. Harrowfield, L. I. Semenova, B. W. Skelton, A. N. Sobolev and A. H. White, *Aust. J. Chem.*, 2020, **73**, 434–446.
41 Y.-S. Yang, M. Liu, Y.-P. Yang, Q.-H. Jin, Z.-F. Li, X.-N. Xue, Z.-J. Zhang and W.-J. Zheng, *Polyhedron*, 2015, **93**, 66–75.
42 L. Xu, N. Pu, Y. Li, P. Wei, T. Sun, C. Xiao, J. Chen and C. Xu, *Inorg. Chem.*, 2019, **58**, 4420–4430.
43 L. Xu, X. Yang, Z. Wang, S. Wang, M. Sun, C. Xu, X. Zhang, L. Lei and C. Xiao, *Inorg. Chem.*, 2021, **60**, 2805–2815.
44 X. Yang, L. Xu, Y. Hao, R. Meng, X. Zhang, L. Lei and C. Xiao, *Inorg. Chem.*, 2020, **59**, 17453–17463.
45 A. Nangia and G. R. Desiraju, *Acta Crystallogr., Sect. A: Found. Crystallogr.*, 1998, **54**, 934–944.
46 J. Liu, L. Chen, H. Cui, J. Zhang, L. Zhang and C.-Y. Su, *Chem. Soc. Rev.*, 2014, **43**, 6011–6061.
47 D. Zhao, D. J. Timmons, D. Yuan and H.-C. Zhou, *Acc. Chem. Res.*, 2010, **44**, 123–133.
48 X. Ma and H. Tian, *Acc. Chem. Res.*, 2014, **47**, 1971–1981.
49 D.-L. Long, E. Burkholder and L. Cronin, *Chem. Soc. Rev.*, 2007, **36**, 105–121.
50 J. Juan-Alcañiz, J. Gascon and F. Kapteijn, *J. Mater. Chem.*, 2012, **22**, 10102–10118.
51 Z.-Q. Wang, L.-Z. Sun, X.-N. Kuang, Y.-L. Lu, Y.-Y. Li, Y.-P. Yang, J.-M. Liu, Y.-Y. Niu and Q.-H. Jin, *Environ. Res.*, 2022, **203**, 111873.
52 Y.-Y. Li, G.-Y. Jin, Z.-Q. Wang, C. Hu, X.-D. Wang, J.-M. Liu, M. Liu, H.-L. Han, Z.-F. Li and Q.-H. Jin, *CrystEngComm*, 2023, **25**, 5851–5860.
53 G.-Y. Jin, L. Zhang, F.-Z. Hu, C. Hu, Y.-L. Lu, Y.-Y. Li, H.-L. Han, J.-M. Liu, Y.-P. Yang, Q.-H. Jin and X.-R. Li, *CrystEngComm*, 2022, **24**, 5307–5316.
54 A. A. Kitos, D. A. Gálico, R. Castañeda, J. S. Ovens, M. Murugesu and J. L. Brusso, *Inorg. Chem.*, 2020, **59**, 11061–11070.
55 W. A. Dar and K. Iftikhar, *Dalton Trans.*, 2016, **45**, 8956–8971.
56 H. Chen, K. Zheng, C. Chen, Y. Zhu, P. Ma, J. Wang and J. Niu, *Inorg. Chem.*, 2022, **61**, 3387–3395.
57 C. S. Cao, S. M. Xia, Z. J. Song, H. Xu, Y. Shi, L. N. He, P. Cheng and B. Zhao, *Angew. Chem., Int. Ed.*, 2020, **59**, 8586–8593.
58 W. Li, L. Liu, X. Li, H. Ren, L. Zhang, M. K. Parvez, M. S. Al-Dosari, L. Fan and J. Liu, *J. Mater. Chem. B*, 2024, **12**, 11800–11809.
59 H. Tian, J. Hong, K. Wang, I. del Rosal, L. Maron, X. Zhou and L. Zhang, *J. Am. Chem. Soc.*, 2017, **140**, 102–105.
60 R.-L. Chen, X.-Y. Chen, S.-R. Zheng, J. Fan and W.-G. Zhang, *Cryst. Growth Des.*, 2013, **13**, 4428–4434.
61 J.-H. Liu, Y.-N. Gu, Y. Chen, Y.-J. Qi, X.-X. Li and S.-T. Zheng, *CrystEngComm*, 2018, **20**, 738–745.
62 Y. Kang, F. Wang and J. Zhang, *Inorg. Chem. Commun.*, 2010, **13**, 938–940.